The Astrophysical Journal, 974:94 (14pp), 2024 October 10 https://doi.org/10.3847/1538-4357/ad65e9

High-latitude Observations of Dissipation-range Turbulence by the Ulysses Spacecraft during the Solar Minimum of 1993–96: The Spectral Break and Anisotropy

Abigale S. Watson[1,2], Charles W. Smith[1], Anastasia V. Marchuk[1], Matthew R. Argall[1], Colin J. Joyce[1], Philip A. Isenberg[1], Bernard J. Vasquez[1], Nathan A. Schwadron[1], and Neil Murphy[3]
[1] Physics Department and Space Science Center, Morse Hall, University of New Hampshire, Durham, NH 03824, USA; abbey@tage.com, Charles.Smith@unh.edu, Anastasia.V.Marchuk@gmail.com, Matthew.Argall@unh.edu, Colin.Joyce@unh.edu, Phil.Isenberg@unh.edu, Bernie.Vasquez@unh.edu, Nathan.Schwadron@unh.edu
[2] Department of Mechanical Engineering, Wentworth Institute of Technology, Boston, MA 02115, USA
[3] Jet Propulsion Laboratory, Mail Stop 180-600, 4800 Oak Grove Drive, Pasadena, CA 91109, USA; Neil.Murphy@jpl.nasa.gov
Received 2024 April 25; revised 2024 July 18; accepted 2024 July 20; published 2024 October 7

Abstract

We examine Ulysses magnetic field observations from 1993 to 1996 as the spacecraft made its first fast-latitude scan from the southern to the northern hemisphere. Most of the observations we use are representative of high-latitude solar minimum conditions. We examine magnetic field power spectra characteristics of interplanetary turbulence at high frequencies, where the spectrum breaks from an inertial range into the ion dissipation range. The onset and spectral index of the dissipation spectrum are consistent with low-latitude observations at 1 au. Both ranges have a ratio of power in perpendicular magnetic field components to parallel components near 3. The power spectrum ratio test developed by Bieber et al. for single-spacecraft analyses that determines the underlying anisotropy of the wave vectors yields only marginally more energy associated with field-aligned wave vectors than perpendicular wave vectors when comparing the inertial and dissipation-range spectra. The lack of significant change in the anisotropies between the inertial and dissipation ranges contrasts strongly with the turbulence found typically for 1 au near-ecliptic observations, where significant differences in both anisotropies are observed.

Unified Astronomy Thesaurus concepts: Fast solar wind (1872); Heliosphere (711)

1. Introduction

The study of solar wind turbulence is an evolving subject, with multiple theories that either of several competing linear and nonlinear dynamics. While the dynamics are not universally agreed to, all theories agree that there exists some form of nonlinear dynamics that transports energy in a conservative manner from large to small scales, where one or more dynamical process dissipates the collective fluctuations of the turbulence to heat the background thermal particles.

The work presented here is part of a larger effort to study solar wind turbulence and the excitation of low-frequency waves by newborn interstellar pickup H^+ and He^+. In the absence of particle energization, these waves are excited at spacecraft-frame frequencies $f_{sc} > f_{i,c}$, where f_{sc} is the fluctuation frequency as measured in the spacecraft frame and $f_{i,c} = e_i B/(2\pi m_i c)$ is the cyclotron frequency of the source ion, e_i is the charge of the ion, B is the mean magnetic field strength, m_i is the ion mass, and c is the speed of light. Waves observed by the Ulysses spacecraft due to pickup H^+ have been analyzed and discussed by Cannon et al. (2013, 2014a, 2014b, 2017) and waves excited by pickup He^+ have been analyzed and discussed by Marchuk et al. (2021). Those studies and others using Advanced Composition Explorer (ACE) and Voyager data (Joyce et al. 2010; Argall et al. 2015, 2017, 2018; Aggarwal et al. 2016; Fisher et al. 2016; Smith et al. 2017; Hollick et al. 2018a, 2018b, 2018c; Ercoline et al. 2023) employed control intervals of solar wind turbulence observations that were without signatures of wave excitation by pickup ions (PUIs). While we employ many of the same techniques used in those papers to identify and analyze intervals of interest, we focus on the control intervals, in an effort to better characterize the solar wind turbulence as observed by the Ulysses spacecraft during the years 1993–1996, in the same manner that we examined solar wind turbulence using the Voyager control intervals (Pine et al. 2020a, 2020b, 2020c, 2020d, 2020e). The Ulysses data used here are from solar minimum years that include the first fast latitude scan.

The present analysis is focused on the properties of the magnetic field power spectrum from the inertial range into the ion dissipation range. The position of the break frequency between the inertial and dissipation ranges is shown to scale with proton inertial length and cyclotron radius, as determined in other studies. Spectra that show no breaks are compared with the predicted position based on the scalings, leading to our conclusion that when the break is not observed it is likely the result of aliasing and proximity to the Nyquist frequency. For those spectra with breaks, the form of the spectrum in each range is fitted with a power law whose index is derived and compared with the energy cascade rate of the turbulence. The index is shown to vary with the cascade rate in a manner observed at low latitudes.

Using mean magnetic field coordinates, the magnetic field components of the power spectra are examined with respect to variance anisotropy and wavevector anisotropy. In these two parameters, important differences emerge from low-latitude fluctuation behavior. At low latitudes, the variance anisotropy, which is the ratio of perpendicular to parallel power components, is smaller in the dissipation range than in the inertial range. Not so, here, at high latitudes, where the ratio remains the same in each range. The wavevector anisotropy is inferred using the ratio of the perpendicular power spectra that models fluctuations containing only wavevectors parallel and

perpendicular to the mean magnetic field (Bieber et al. 1996). For low latitudes, the Bieber test shows that the dissipation range has a larger fraction of power in fluctuations with wavevectors along the mean magnetic field as compared to the inertial range. At high latitudes, only a marginal difference, but still larger, is found.

The outline of the paper is as follows. Section 2 describes the methods used to obtain a spectrum and Section 3 shows the spectra forms obtained. The behavior of the spectral break is characterized in Section 4 and the spectral index is characterized in Section 5. Section 6 examines the variance anisotropy, and Section 7 examines the wavevector anisotropy. The differences found between low- and high-latitude observations is discussed in Section 8, and Section 9 summarizes the results.

2. Data Analysis Methods

Our study makes use of the power and polarization analyses that are often used in studies of waves due to newborn interstellar PUIs and shock-accelerated particles (Joyce et al. 2010; Cannon et al. 2014a, 2014b; Argall et al. 2015, 2017, 2018; Aggarwal et al. 2016; Fisher et al. 2016; Smith et al. 2017; Hollick et al. 2018a, 2018b, 2018c; Marchuk et al. 2021). The ensemble of data intervals was first assembled by computing both the power and polarization spectra (Fowler et al. 1967; Means 1972; Mish et al. 1982) of intervals that appear to be stationary by eye, but lacking shocks, isolated current sheets, and similar strong signals that would obscure the underlying turbulent characteristics. However, instead of focusing on data intervals that exhibit wave characteristics, we observe polarization spectra to identify and exclude data intervals that contain waves attributable to newborn PUIs and other suprathermal ion sources, such as shocks, as was done in Watson et al. (2022).

The analysis described here presents the computation of power spectra only via prewhitened Blackman–Tukey analysis techniques (Blackman & Tukey 1958; Matthaeus & Goldstein 1982a; Chen 1989; Leamon et al. 1998a; Smith et al. 2006a, 2006b; Hamilton et al. 2008; Hollick et al. 2018a; Pine et al. 2020a, 2020b, 2020c, 2020d; Marchuk et al. 2021). The Blackman–Tukey method computes the power spectrum by performing a Fourier transform of the autocorrelation function (Blackman & Tukey 1958; Matthaeus & Goldstein 1982a, 1982b). Fundamental concepts of hydrodynamic (HD) turbulence lead to the use of this definition naturally (Batchelor 1953). Utilizing a first-order difference filter to prewhiten the data prior to computing the autocorrelation function reduces spectral leakage, thereby better resolving changes in spectral slope. However, this also flattens the computed spectrum. This must be corrected for by using a post-darkening filter after the spectrum is computed in order to return the computed spectrum to the true underlying form (Chen 1989). The analyses shown here build upon turbulence studies using the Wind (Leamon et al. 1998a), ACE (Smith et al. 2006a, 2006b; Hamilton et al. 2008), Voyager (Pine et al. 2020a, 2020b, 2020c, 2020d), and Ulysses (Watson et al. 2022) spacecraft.

To perform the analyses described here, we use high-resolution magnetic field data from the Ulysses/FluxGate Magnetometer instrument. To supplement this analysis, we use hourly averages of thermal proton moments (wind velocity, density, and temperature) from the Ulysses/Solar Wind Observations over the Poles of the Sun (SWOOPS) instrument.

3. Data Overview

Figure 1 shows the computed power spectra for four representative intervals of magnetic field data recorded by the Ulysses spacecraft during the four years studied here. The power spectra are computed in mean field coordinates defined by $\hat{\boldsymbol{X}} \equiv (\boldsymbol{B} \times \hat{\boldsymbol{R}})/|\boldsymbol{B} \times \hat{\boldsymbol{R}}|$, $\hat{\boldsymbol{Y}} \equiv (\boldsymbol{B} \times (\boldsymbol{B} \times \hat{\boldsymbol{R}}))/|\boldsymbol{B} \times (\boldsymbol{B} \times \hat{\boldsymbol{R}})|$, and $\hat{\boldsymbol{Z}} \equiv \boldsymbol{B}/|\boldsymbol{B}|$, where $\boldsymbol{B}$ is the mean magnetic field vector averaged over the data interval and $\hat{\boldsymbol{R}}$ is the radial unit vector from the Sun to the point of measurement (Belcher & Davis 1971; Bieber et al. 1996). Each interval shows the computed diagonal elements of the power spectral density (PSD) matrix P_{XX}, P_{YY}, and P_{ZZ}. In addition, we show the trace of the PSD $P_{\rm Tr}$, which is independent of the coordinate system used, and the spectrum of the time series of the magnitude of the magnetic field P_M. In each instance, P_M is the lowest-amplitude spectrum in the plot, with P_{ZZ} the next highest. P_{XX} and P_{YY} are consistently the highest power levels for the individual components, and $P_{Tr} = P_{XX} + P_{YY} + P_{ZZ}$ is the highest spectrum, being the total magnetic energy in the fluctuation. We employ mean field coordinates to compute the power spectra, because the power in the fluctuations parallel to the mean magnetic field when compared to the trace power is a measure of the compression of the fluctuations. These same spectra can be used to analyze the distribution between the underlying wavevectors parallel and perpendicular to the mean field (Bieber et al. 1996), as described below.

We attempt to fit the inertial and dissipation ranges separately for each spectrum computed. The fits are represented by the red lines.

Figure 1 (top left) shows our analysis for day-of-year (DOY) 350 of 1993 from 00:00 to 12:00 UT when $R_{\rm AU} = 3.91$ au and $\Theta_{\rm lat} = -46.^{\circ}9$. In this example, we find a very weak break in the power spectra marking the onset of dissipation at ∼0.1 Hz. There are other instances in this paper when a spectral break cannot be found. Other signs of dissipation are present, including a convergence of P_M with $P_{\rm Tr}$ and a negative bias in the magnetic helicity at $f_{\rm sc} > 0.05$ Hz (not shown). This guides our frequency range selection for fitting the inertial and dissipation ranges, where we obtain spectral indices of −1.62 and −1.90, respectively. There is a mild degree of aliasing at $f_{\rm sc} > 0.2$ Hz.

Figure 1 (top right) shows our analysis of DOY 009 of 1994 from 12:00 to 20:00 UT when Ulysses is at $R_{\rm AU} = 3.78$ au and $\Theta_{\rm lat} = -49.^{\circ}3$. In this case, a very strong spectral break is observed at ∼0.1 Hz in all three components of the magnetic spectrum, as well as the trace. This makes it easy to select inertial and dissipation-range frequencies to fit where we find the inertial and dissipation-range spectral indices to be −1.66 and −2.86, respectively. As before, the individual components follow similar spectral forms, while the spectrum P_M is more shallow and converges to within an order of magnitude of $P_{\rm Tr}$ in the dissipation-range frequencies.

The two examples in the bottom row of Figure 1 are from data recorded north of the heliospheric current sheet. Figure 1 (bottom left) shows our analysis for DOY 196 of 1995 from 15:00 to 23:00 UT, recorded closest to perihelion at $R_{\rm AU} = 1.91$ au and $\Theta_{\rm lat} = 78.^{\circ}6$. Here we again see a strong spectral break at ∼0.16 Hz. We use the method described below to compute the break frequency. In most regards, the results are similar to those in the top row, with aliasing beginning at ∼0.4 Hz. The inertial (dissipation-) range spectral index determined by the fit is −1.60 (−3.24).

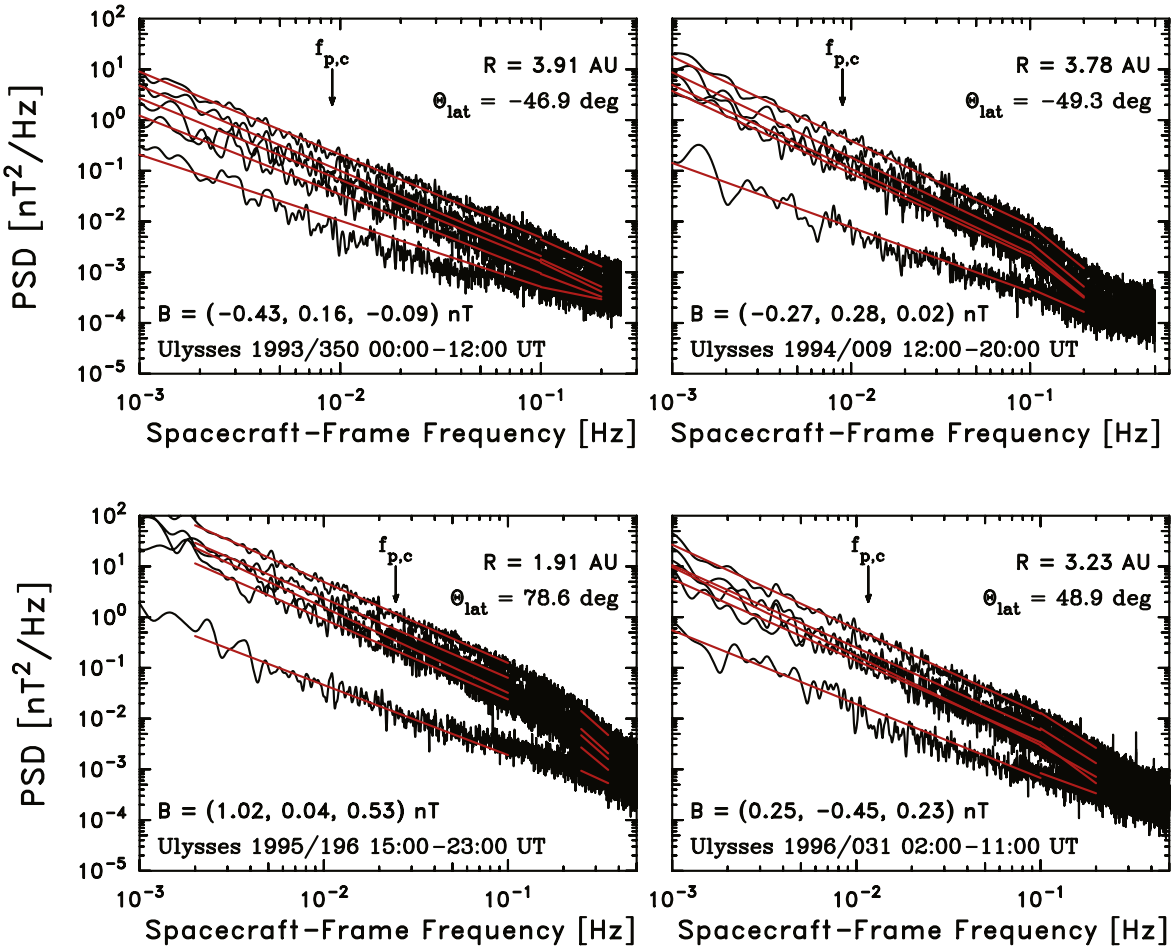

Figure 1. Four examples of the types of inertial range and dissipation-range spectra seen in this study. Each panel gives the time interval, mean magnetic field vector, heliocentric distance, and heliolatitude. The proton cyclotron frequency is marked. We show the computed PSD for the $\hat{R}$, $\hat{T}$, and $\hat{N}$ components of the measured magnetic field. We also show the trace (total) spectrum and the spectrum of the $|\boldsymbol{B}|$, which is the lowest power spectrum in each case. The upper row of two examples corresponds to spacecraft locations south of the heliospheric current sheet. The bottom row of two examples corresponds to spacecraft locations north of the heliospheric current sheet.

Figure 1 (bottom right) shows our analysis for DOY 031 of 1996 from 02:00 to 11:00 UT. The spacecraft is positioned at $R_{\rm AU} = 3.23$ au and $\Theta_{\rm lat} = 48.^{\circ}9$. A spectral break is again seen at $\sim$0.1 Hz with an inertial (dissipation-) range index -1.6 (-2.30).

Multiple theories exist to explain the spectral break and resulting steepening of the power spectrum at higher frequencies, but most agree that it marks the onset of dissipation by thermal ions by one or more mechanisms (Leamon et al. 1998a; Markovskii et al. 2008, 2015, 2016; Chen et al. 2010b, 2014; He et al. 2011; Šafránková et al. 2013; Bruno & Trenchi 2014; Woodham et al. 2018, 2021). We will pay particular attention to those spectra that do not display a spectral break in an effort to resolve whether dissipation does not occur or is simply unresolved by the measurement.

Figure 2 shows the average plasma parameters for each of the events studied. Here and throughout the paper, the red triangles represent intervals where a clear spectral break is seen, while the black circles represent intervals where no spectral break is readily evident. Parameters involving the magnetic field alone are obtained by averaging the high-cadence magnetic field data for the exact interval studied. Parameters describing the thermal ion population (wind speed, density, and temperature) are obtained from 1 hr averages of the SWOOPS data. Parameters requiring both magnetic field and thermal ion data are computed using the above averages.

From top to bottom, Figure 2(a) gives the spacecraft location in heliocentric distance $R_{\rm AU}$ (solid line) and heliographic latitude $\Theta_{\rm lat}$ (dashed line). Figure 2(b) shows the mean magnetic field strength B as computed from the high-cadence data. Figure 2(c) shows the angle between the mean magnetic field and radial direction Θ_{BR} as computed from the average vector components of $\boldsymbol{B}$ using the high-cadence data. Figure 2(d) presents the average wind speed $V_{\rm SW}$ as computed from the hourly resolution SWOOPS data. Figure 2(e) gives the average thermal proton density N_P as computed from the hourly SWOOPS data. Figure 2(f) shows the average proton temperature T_P as computed from the hourly SWOOPS data. Figure 2(g) displays the thermal proton $\beta_P \equiv V_{\rm th}^2 V_{\rm A}^{-2} = (3.47 \times 10^{-5}) N_P T_P / B^2$, where $V_{\rm th}$ is the thermal speed of a proton with temperature T_P and the Alfvén speed $V_{\rm A} \equiv B(4\pi\rho)^{-1/2} = 21.8 B (N_P)^{-1/2}$, where ρ is the mass density of protons. As above, we compute those parameters requiring both magnetic field and thermal ion data by using the average of each. Figure 2(h) gives the Alfvén speed as defined above. Last, Figure 2(i) shows the average Alfvén Mach number $M_{\rm A} \equiv V_{\rm SW}/V_{\rm A}$.

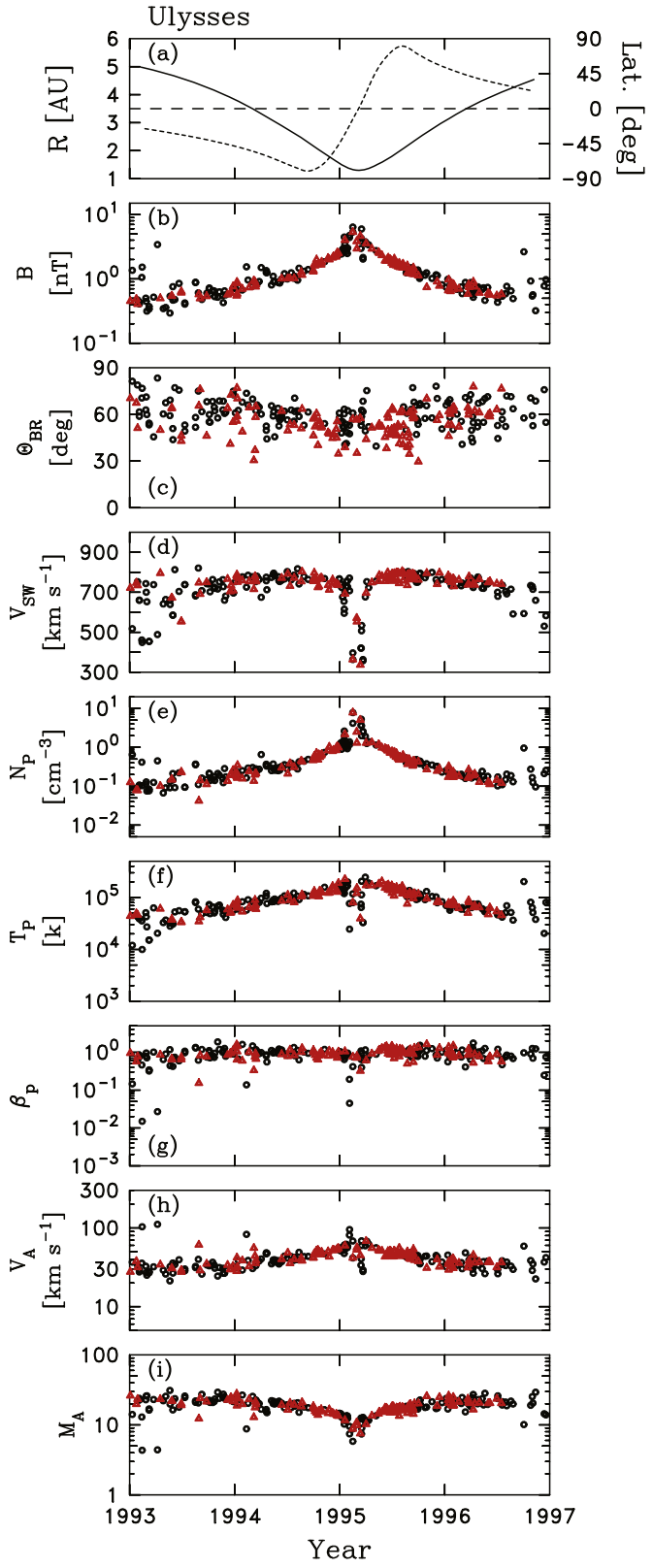

Figure 2. Ambient plasma parameters as measured by the Ulysses spacecraft from 1993 through 1996. The red triangles represent those intervals that show clear evidence of a spectral break at dissipation scales, and the black circles represent intervals that do not. From top to bottom, we plot the trajectory heliodistance and heliolatitude, the average magnetic field intensity B, the angle between the mean field and the radial direction Θ_{BR}, the mean solar wind speed $V_{\rm SW}$, the thermal proton density N_P, the thermal proton density T_P, the proton energy density parameter β_P, the Alfvén speed $V_{\rm A}$, and the Alfvén Mach number $M_{\rm A}$.

The general parameters of the local plasma offer no surprises, as they are typical of solar wind parameters at these locations at solar minimum. Except for a small number of low-latitude events, most of the variation observed is the result of changing $R_{\rm AU}$. What is notable in Figure 2 is that the intervals where a clear spectral break is observed possess the same plasma parameters as those where no clear spectral break is found. While B, Θ_{BR}, $V_{\rm SW}$, and N_P are described by Parker's original treatment of the solar wind (Parker 1963), T_P is not described by adiabatic expansion and is the result of in situ heating driven by the turbulence (Watson et al. 2022).

4. Spectral Break

We have stated above that the ensemble of spectra used here are divided approximately equally between spectra that show a clear spectral break, indicating the onset of dissipation, and those that do not. We would like to understand why some events do not show the spectral break that is expected, and we would like to find a way to employ those events reliably in a study of dissipation-range characteristics.

Figure 1 shows a high degree of consistency between the spectral break frequency throughout the data. Likewise, Figure 2 shows smooth curves with relatively little variability in the plasma parameters. It is desirable to have variation in the turbulence properties and plasma conditions in order to find the underlying physics that leads to the onset of dissipation. While this will prove difficult in this instance, the high degree of uniformity will permit us to model the onset of dissipation with a high degree of accuracy for the data intervals studied here. This is due to the fact that the leading parameters controlling dissipation are strongly correlated at high latitudes during solar minimum conditions. Simply stated, all leading theories produce the same prediction.

Figure 3 compares the spectral break frequency $f_{\rm break}$ with several familiar predictive quantities. We use only those data intervals that show a recognizable break in the power spectrum. Figure 3 (top) compares $f_{\rm break}$ to $f_{p,c}$. There is general agreement in the trend, but with considerable scatter. As a general scaling, $f_{\rm break} \simeq 7 f_{p,c}$.

Figure 3 (middle) compares $f_{\rm break}$ to $f(L_{p,c})$, where $L_{p,c}$ is the proton Larmor radius,

$$L_{p,c} = V_{\rm th}(2\pi f_{p,c})^{-1}, \quad (1)$$

and the spacecraft-frame frequency derived from convecting the proton Larmor radius past the spacecraft is given by

$$f(L_{p,c}) = V_{\rm SW}/L_{p,c}. \quad (2)$$

There is again considerable spread in the results, but on average $f_{\rm break} \simeq f(L_{p,c})/10$.

Figure 3 (bottom) compares $f_{\rm break}$ to $f(L_{p,i})$, where $L_{p,i}$ is the proton inertial scale,

$$L_{p,i} = V_{\rm A}(2\pi f_{p,c})^{-1}, \quad (3)$$

and the spacecraft-frame frequency derived from convecting the proton inertial scale past the spacecraft is given by

$$f(L_{p,i}) = V_{\rm SW}/L_{p,i}. \quad (4)$$

As above, there is a significant amount of scatter, but on average $f_{\rm break} \simeq f(L_{p,i})/10$.

The strong similarity between the bottom two panels of Figure 3 can be traced to $\beta_P \simeq 1$ in Figure 2. Figure 4 compares

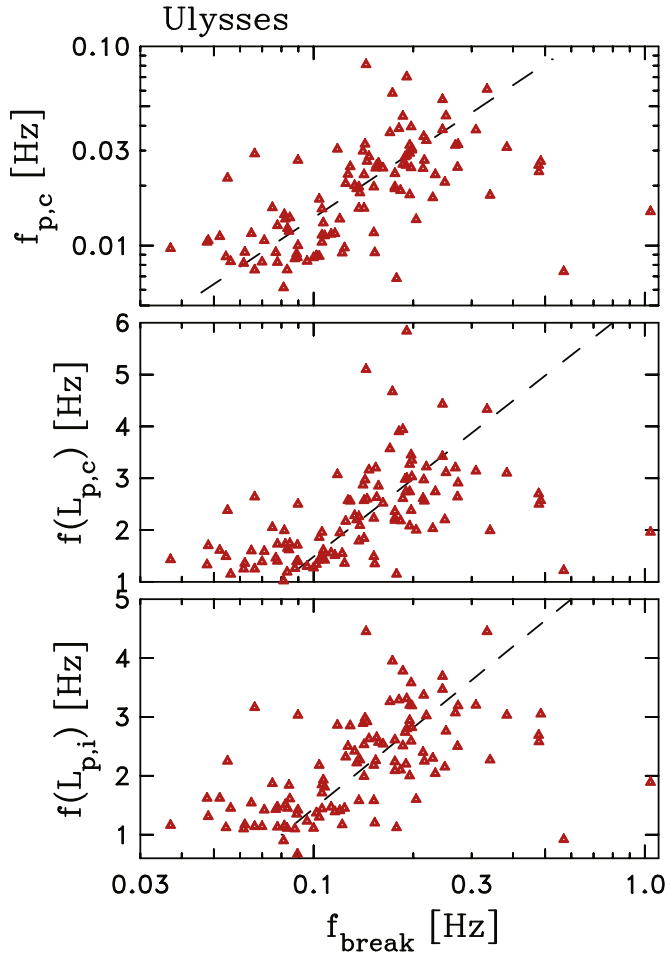

Figure 3. The proton cyclotron frequency and the spacecraft-frame frequencies associated with the convection of the proton Larmor radius and proton inertial scale plotted as a function of the spectral break associated with the onset of dissipation.

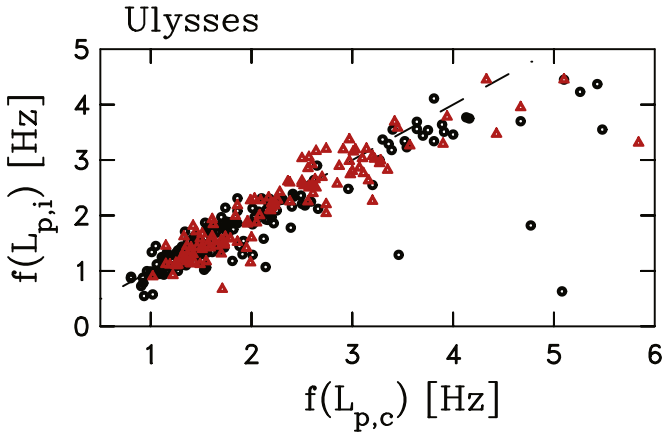

Figure 4. Comparison of the frequencies associated with the convection of the proton Larmor radius and proton inertial scales.

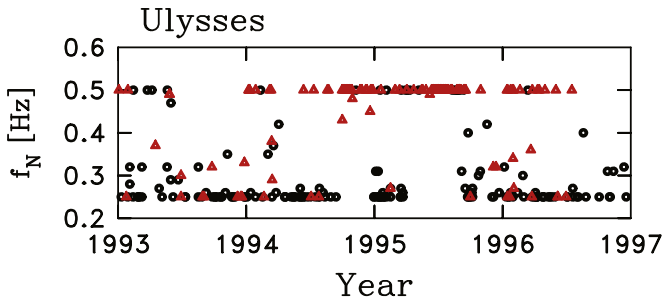

Figure 5. Nyquist frequency for each data interval plotted as a function of time. In keeping with Figure 2 and elsewhere throughout the paper, the red triangles represent those intervals that show clear evidence of a spectral break at dissipation scales and the black circles represent those intervals that do not.

$f(L_{p,c})$ and $f(L_{p,i})$. Again, the red triangles (black circles) represent spectra that do (do not) display spectral breaks associated with dissipation. There are three examples with $f(L_{p,c}) \gg f(L_{p,i})$ that are not shown. The average behavior shows $f(L_{p,c}) \simeq f(L_{p,i})$, with a few of the spectra that are not showing breaks residing farther off the line of unity than the spectral break examples, but for the most part both populations possess the same range of $L_{p,i} = L_{ic}$. Because of this, we are unable to distinguish between the different predictors for the onset of dissipation. However, we can reliably predict $f_{\rm break}$ by using either predictor.

One desirable result that derives from the consistently large values of Θ_{BR} throughout this analysis is that the reported dependence of $f_{\rm break}$ upon Θ_{BR} is not a significant factor in our analysis (Bruno & Trenchi 2014).

It should be possible to use any of these scalings to provide a measure of the onset of dissipation in those cases where a clear spectral break is not observed. However, in order to rule out the possibility that these are instances where a different dissipation mechanism is active, we will attempt to find another correlation that may indicate a distinction between those spectra showing a dissipation break and those that do not.

When characterizing the dissipation-range spectra for those intervals where a clear spectral break is observed, we can use the observed frequency interval associated with dissipation to select a frequency range for analysis. In order to establish a reliable frequency interval to represent the dissipation range when a clear spectral break is not observed, we turn to the above scalings. However, there is a further limitation in that the Nyquist frequency $f_{\rm N} = (2\delta)^{-1}$, which is the highest frequency that can be resolved given the cadence of the measurement δ, varies between 0.2 and 0.5 Hz. Figure 3 clearly indicates that it is likely that many of the spectra that are observed to lack a spectral break in association with dissipation do so because $f_{\rm N}$ is too small to permit the resolution of this part of the spectrum.

Figure 5 plots the computed Nyquist frequency for each data interval studied. The spectra exhibiting a spectral break predominantly have $f_{\rm N} = 0.5$ Hz, while those without a spectral break are more often $f_{\rm N} = 0.25$ Hz. If we add to that the frequency where the onset of aliasing is observed, less than half of the spectra seen to be without a spectral break have the potential for observing the spectral break if the average scaling seen in Figure 3 is applied. Add to this the factor of 2 spread in the observations and it becomes clear that the vast majority of spectra seen without a spectral break are unable to resolve the break due to the Nyquist frequency and aliased power. For this reason, we will omit from this point on any discussion of spectra that fail to exhibit a spectral break in association with dissipation when examining the dissipation-range spectrum and limit the analysis to the 119 spectra showing clear evidence of dissipation in the magnetic power spectra.

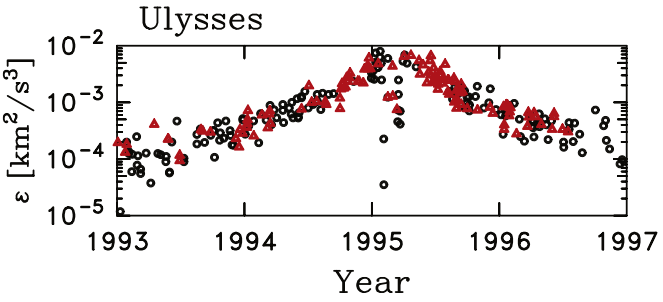

Figure 6. Computed rate of energy transport through the inertial range as determined at 10 mHz using Equation (5) and the computed trace of the magnetic PSD matrix plotted as a function of year.

5. Spectral Index

In past studies at 1 au, there is an indication that the steepness of the power spectrum in the dissipation range depends on the computed rate of energy transport through the inertial range. We compute the rate of energy transport according to magnetohydrodynamic (MHD) extensions of HD theory. We use a modified version of the Kolmogorov expression suitable for MHD:

$$\epsilon = \frac{f_{sc}^{5/2}\,[E(f_{sc})]^{3/2}\cdot 21.8^3}{V_{SW}N_P^{3/2}}, \tag{5}$$

where $E(f_{sc})$ is the measured magnetic field PSD in units of nT^2 Hz^{-1}. The terms N_P and 21.8^3 are part of the conversion of the magnetic field to Alfvén units. We assume equipartition of kinetic and magnetic energy, so that the Alfvén ratio $R_A = 1$. R_A enters the expression through $E(f_{sc})$ and is generally measured to be in good agreement with this assumption. By this expression, ϵ is given in units of km^2 s^{-3}. Equation (5) has been proven to yield excellent agreement with heating rates at 1 au (Vasquez et al. 2007), third-order theory at 1 au (Stawarz et al. 2009), transport theory when applied to Voyager 1 and 2 data (Pine et al. 2020d), and transport theory when applied to this same data set (Watson et al. 2022).

Equation (5) derives from MHD extensions of the HD prediction for the power spectrum. HD theory predicts that the amplitude of the omnidirectional power spectrum (the spectrum integrated over constant magnitude of wavevector k) is determined by the rate of energy transport (Kolmogorov 1941):

$$P(k) = A_K\,\epsilon^{2/3}k^{-5/3}. \tag{6}$$

The prediction that $E(f_{sc})$ varies as $f_{sc}^{-5/3}$ is a good approximation to what we observe in this study (Watson et al. 2022).

The stronger the turbulent transport, the steeper the dissipation spectrum becomes. A previous analysis concluded that this was partly the result of including data intervals taken from magnetic clouds (Smith et al. 2006a). Examination of Voyager 1 data from 1 to 10 au supported this interpretation, but the analysis of Voyager 2 data from 1 to 45 au failed to support this conclusion (Pine et al. 2020a).

Figure 6 plots the rate of energy transport through the inertial range as a function of time. Since the analysis of the energy transport rate is based on inertial range frequencies, we include those spectra that fail to show a discernible spectral break associated with dissipation. It appears that the two populations

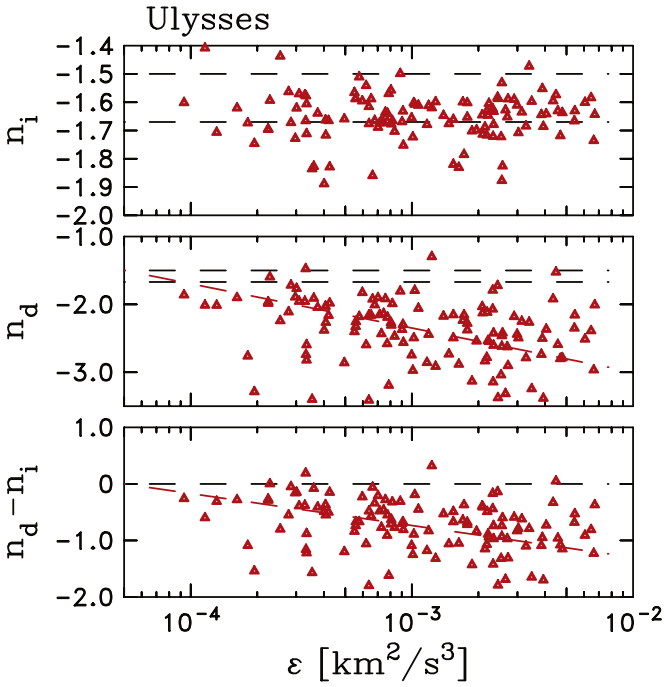

Figure 7. Fit spectral index to P_{Tr} for the inertial range (top), dissipation range (middle), and the difference (bottom), shown as a function of the energy transport rate through the inertial range.

are uniformly distributed through the data. There is a systematic change of ϵ through this part of the trajectory, but there is no tendency to find high or low values of ϵ leading to isolation of the two spectral types in different parts of the trajectory. This further demonstrates that whatever the explanation is for the two populations of computed spectra, there is no distinction based on the strength of the nonlinear energy transport through the inertial range and associated heating of the plasma.

Figure 7 (top) shows the fit inertial range indexes of P_{Tr} plotted as a function of the rate of energy transport through the inertial range. The horizontal dashed lines at $-3/2$ and $-5/3$ represent predictions from the two leading theories for the inertial range index (Kolmogorov 1941; Iroshnikov 1964; Kraichnan 1965). There are also theories that hybridize these views (Goldreich & Sridhar 1995; Boldyrev 2006). Analysis of near-ecliptic observations from $R_{AU} \simeq 1$ au support the theory represented by Equation (6) that leads to a spectral index of $-5/3$ (Kolmogorov 1941; Matthaeus & Zhou 1989; Leamon et al. 1999; Vasquez et al. 2007) and this value does appear to better represent the clustering of inertial range indices shown here. However, as is seen at 1 au, there is ample spread in the distribution. This range of values generally provides a good description of the results extending out to ~40 au (Pine et al. 2020b).

Figure 7 (middle) shows the fit dissipation-range indexes of P_{Tr} plotted as a function of the rate of energy transport through the inertial range. A greater range of values for n_d is expected relative to what is seen for n_i (Leamon et al. 1998a). The spectra are seen to steepen with increasing values of ϵ, as has been seen in ACE data at 1 au (Smith et al. 2006a; Bruno et al. 2014).

Given that there is some variation in the spectral index of the inertial range, it is worth verifying that the steepening implied

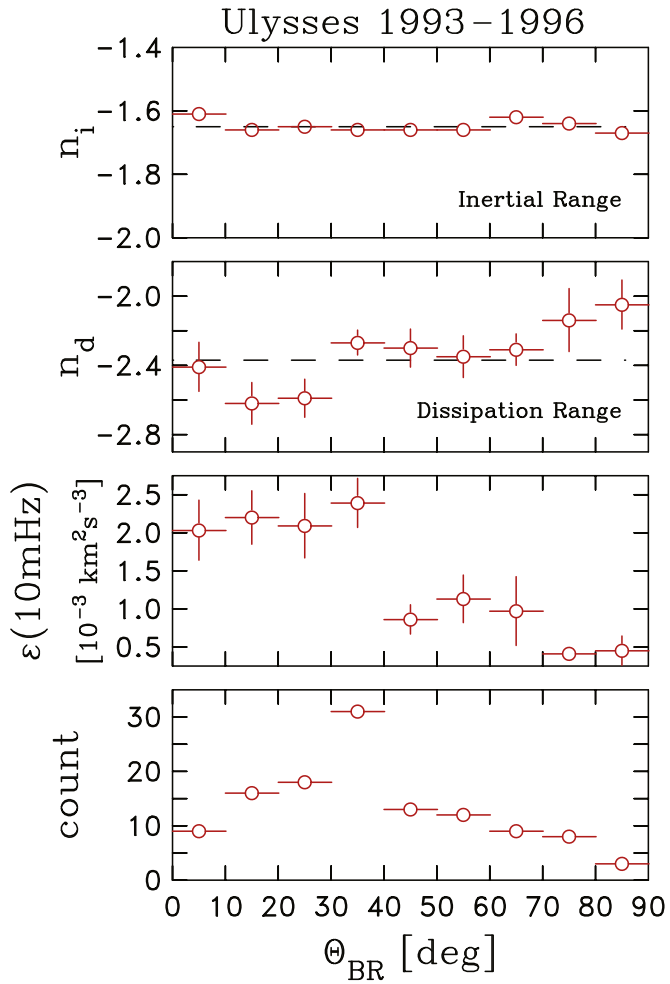

Figure 8. Analysis of spectra that do exhibit steepening in association with dissipation. The mean spectral index for the trace of the magnetic PSD matrix as computed for 10° bins of Θ_{BR} with the error of the mean represented as vertical lines on the symbols. In addition, the computed rate of energy transport through the inertial range as derived from the trace spectrum at 10 mHz and the number of data intervals in each angular bin are shown. Overall averages are represented by horizontal dashed lines that also reflect the width of the bins. The computed uncertainties are represented by vertical lines that are sometimes smaller than the symbols used.

by the top two panels is real. Figure 7 (bottom) shows the difference between the two spectral indexes. The difference is significant and the difference is again seen to increase with ϵ.

The underlying geometry of the turbulence is often discussed as having two components where there are wavevectors aligned with the mean magnetic field and others that are perpendicular to it (Matthaeus et al. 1990; Bieber et al. 1996; Dasso et al. 2005; Hamilton et al. 2008; Forman et al. 2011; Pine et al. 2020c; Watson et al. 2022). If the expected nonlinear or dissipation dynamics of the turbulence dominates in only one component, then it might be expected that the spectral characteristics may depend on the orientation of the mean magnetic field relative to the radial (solar wind flow) direction. Figure 8 plots our analysis of those data intervals that show a clear spectral break and steepening at dissipation scales. The plot of the average spectral index of the inertial range n_i as a function of Θ_{BR} shows no significant dependence upon Θ_{BR}. The horizontal dashed line marks −1.65.

The plot of the average spectral index of the dissipation range n_d in Figure 8 does show a dependence upon Θ_{BR}, with

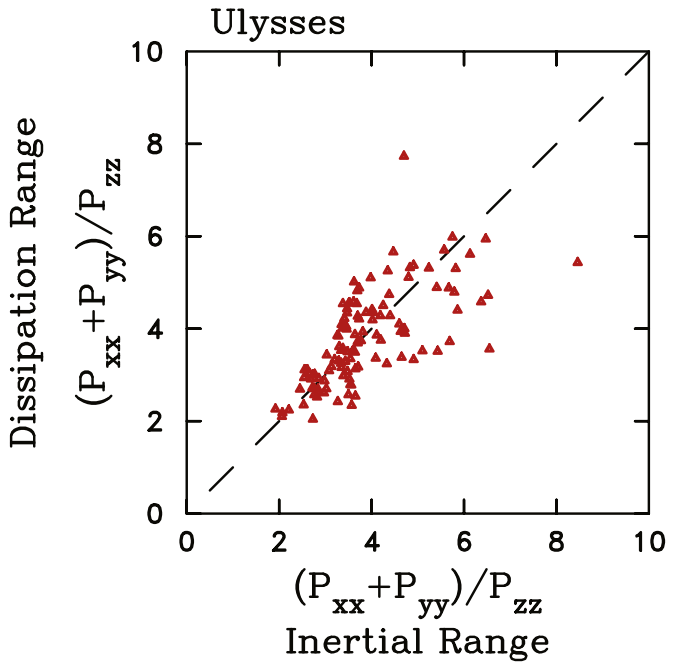

Figure 9. Comparison of the variance anisotropy in the inertial and dissipation ranges.

the more shallow examples associated with larger values of Θ_{BR}. The horizontal dashed line in the left column is set at −2.37, which is the average value of n_d in the ensemble. This may signify an anisotropy in the dissipation processes, but another explanation is possible. The plot of the average value of energy transport through the inertial range ϵ as shown in Figure 8 exhibits similar behavior, with stronger turbulence levels for $\Theta_{BR} < 40°$. This could be, in part, due to the decreasing strength of the turbulence with increasing heliocentric distance, but is also consistent with Figures 2 and 6 and the results from 1 au where the more shallow dissipation-range spectra are associated with the weaker turbulence levels.

The bottom panel of Figure 8 gives the number of data intervals used in each 10° bin of Θ_{BR}. The bin $\Theta_{BR} > 80°$ is underrepresented. The bins $0° < \Theta_{BR} < 80°$ are sufficiently populated to sustain the above conclusions.

6. Variance Anisotropy

The variance anisotropy as defined by the ratio of power in the perpendicular and parallel components of the spectrum $(P_{XX} + P_{YY})/P_{ZZ}$ is a long-standing proxy measurement for the degree of compression of the fluctuations and has traditionally been used as an indication of the presence of Alfvén waves (Belcher & Davis 1971).

Figure 9 compares the variance anisotropy of the inertial range at 10 mHz and the dissipation range at 0.2 Hz. On average, the anisotropy may be slightly higher in the inertial range, but the difference is small and the spread in results is too great to make this statement in a definitive manner. This is unexpected, as the 1 au low-latitude results show that the anisotropy in the dissipation range is less than in the inertial range (Hamilton et al. 2008). In both cases, the dissipation range magnetic fluctuations are more nearly isotropic in nature (Oughton et al. 2015).

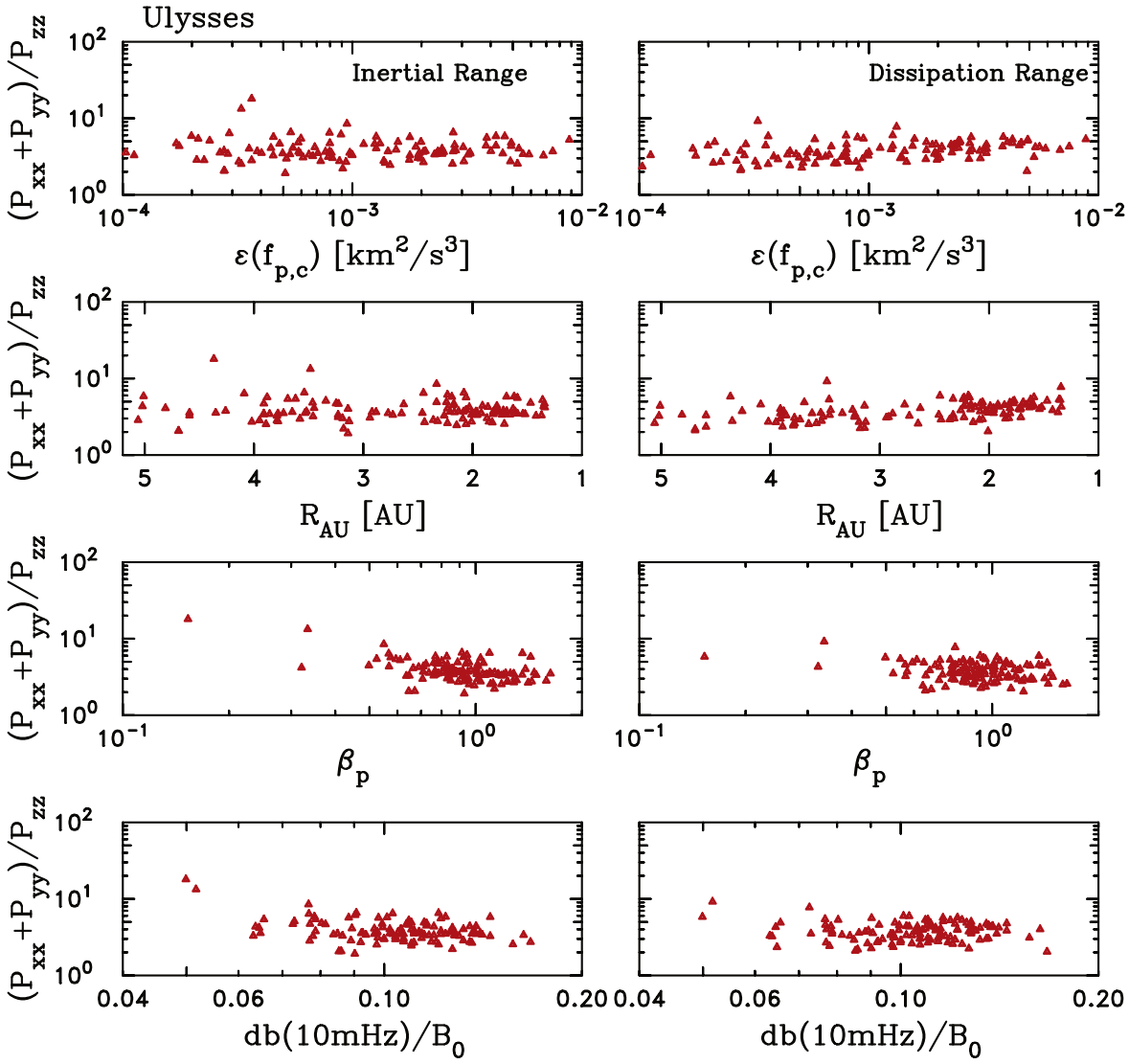

Figure 10. Variance anisotropy $(P_{XX} + P_{YY})/P_{ZZ}$ plotted as a function of the energy transport through the inertial range as computed for the proton cyclotron frequency $f_{p,c}$, heliocentric distance, the thermal proton pressure parameter β_P, and the fluctuation amplitude at 10 mHz normalized by the mean field strength, for the inertial range frequencies (left) and dissipation-range frequencies (right). See the text for explanation.

Figure 10 plots the variance anisotropy in the inertial range (left) and dissipation range (right) as a function of four different parameters. Figure 10 (top row) plots the anisotropy as a function of the energy cascade rate evaluated at the proton cyclotron frequency $\epsilon(f_{p,c})$. The frequency range over which the anisotropy averages are computed varies according to the duration of the data interval, the Nyquist frequency, any possible aliasing at high frequencies, and the overall range of resolved frequencies used to determine the spectral index fit. However, the ranges were chosen to accurately represent the high-frequency extent of the inertial range and the dissipation range before the onset of noise domination or aliasing. There is no clear trend in the variation of the anisotropy within the inertial range, but a mild dependence of the dissipation-range anisotropy upon ϵ is seen, with the anisotropy increasing with the energy cascade rate.

Figure 10 (second row) plots the variance anisotropy as a function of decreasing heliocentric distance. Again, there is no variation in the anisotropy of the inertial range, but there is a mild dependence for the dissipation-range result. The dependence upon R mimics the dependence upon ϵ as expected, because ϵ declines with increasing R.

Figure 10 (third row) plots the variance anisotropy as a function of the thermal proton β_P. There is an implied dependence with the anisotropy decreasing with increasing β_P that is consistent with previous low-latitude studies (Smith et al. 2006c; Pine et al. 2020c), but this conclusion shown here depends on the very few low-β_P results and disregards the values at $\beta_P > 1$. However, it is just as valid to focus on the results for $\beta_P > 0.7$ that imply there is no dependence upon β_P. A greater range of β_P is needed, but as Figure 2 shows, β_P is nearly constant over this part of the Ulysses orbit and further demonstrates the uniformity of high-latitude plasma parameters during solar minimum.

Figure 10 (bottom row) plots the variance anisotropy as a function of the fluctuation amplitude at 10 mHz as determined from the fit power spectrum normalized by the mean field strength. This is a bit more complicated than the row above it. At $dB/B_0 > 0.06$, the anisotropy appears flat. The two spectra at $dB/B_0 < 0.06$ do not carry sufficient statistics to imply any significant dependence of the variance anisotropy upon

fluctuation level. This is seen in both the inertial and dissipation ranges. Since the power level is a primary contributor to ϵ, along with the density and wind speed that vary independently over the orbit, this bottom panel demonstrates the importance of energy transport rather than the simpler measurement of the power spectrum.

One might speculate that the different behavior for $dB/B_0 \lesseqgtr 0.06$ and some of the other parameters shown in Figure 10 could be the result of the measured spectrum reaching a noise floor for the instrument, but this is not the case. Since $P_{ZZ} <$ both P_{XX} and P_{YY}, a noise floor would decrease the anisotropy with decreasing power level, which is the reverse of what is seen.

Although we have searched for any dependence that will illuminate an underlying behavior of the variance anisotropy, the leading-order conclusion of this analysis is that the inertial and dissipation-range anisotropies are essentially identical for this data set with a value $\simeq 3$. The exceptions to this result are data intervals with the weakest spectra and $\beta_P < 0.5$ that have greater anisotropies. Furthermore, there is a high degree of uniformity across the data set, despite the range in heliocentric distance spanned by the years analyzed here. We attribute this to the fact that the physical parameters show a high degree of uniformity at high latitudes during solar minimum. This is especially true of parameters that are constructed as ratios of relevant physical measurements that may affect dissipation dynamics such as β_P.

7. Wavevector Anisotropy

Single-spacecraft studies of solar wind turbulence are limited by the necessary use of the Taylor frozen-in-flow approximation (Taylor 1935):

$$f_{sc} = (2\pi)^{-1} \boldsymbol{k} \cdot \boldsymbol{V}_{SW}, \tag{7}$$

where the relevant spatial scale is assumed to be convected past the spacecraft faster than it evolves. This yields a measure of spatial dependence along the flow only, which is the radial direction. It effectively integrates the three-dimensional (3D) structures across the flow, while assuming that all dynamics are effectively zero. Measurements of this type have been used to infer a likely 3D structure. For instance, the transverse nature of magnetic and velocity fluctuations together with the low degree of density fluctuations led Belcher & Davis (1971) to conclude that the fluctuations had characteristics that were consistent with parallel-propagating Alfvén waves.

Simulations of incompressible MHD turbulence have shown that nonlinear dynamics transport energy toward wavevectors that are perpendicular to the mean magnetic field, creating a 2D nonlinear system (Shebalin et al. 1983; Oughton et al. 1994; Goldstein et al. 1995; Matthaeus et al. 1996a, 1998, 2016; Cho & Vishniac 2000; Müller & Grappin 2005; Horbury et al. 2008; Boldyrev et al. 2009; Parashar et al. 2009; Chen et al. 2010a; Beresnyak 2011; Forman et al. 2011; Markovskii & Vasquez 2011; Servidio et al. 2012, 2014, 2015; Vasquez & Markovskii 2012; Valentini et al. 2016). Since 2D magnetic fluctuations are perpendicular to the mean field, the 2D model can also be used to explain the observations of Belcher & Davis (1971), as well as what is shown here in Figures 9 and 10. Multispacecraft studies using the Cluster and Magnetospheric MultiScale constellations are able to avoid the Taylor approximation to obtain the true orientation of the wavevector $\boldsymbol{k}$ and have produced several different turbulence models, depending on the data interval selected. Kinetic Alfvén waves are one popular wave-based nonlinear dynamic that is supported by some multiplatform analyses (Bale et al. 2005; Howes et al. 2008; Sahraoui et al. 2009, 2010; Howes & Quataert 2010; TenBarge et al. 2013; Hughes et al. 2017; Isenberg & Vasquez 2019).

One method available for separating the energy content of parallel and perpendicular wavevectors is based upon a well-established formalism for the correlation function in HD turbulence (Bieber et al. 1996). Assuming that the 3D power spectrum can be divided into parallel and perpendicular wavevectors only (an approximation to reality), it is possible to write:

$$\frac{P_{YY}}{P_{XX}} = \frac{k_{1D}^{1-|n_i|} + r'\left(\frac{2\,|\,n_i\,|}{1+|\,n_i\,|}\right)k_{2D}^{1-|n_i|}}{k_{1D}^{1-|n_i|} + r'\left(\frac{2}{1+|\,n_i\,|}\right)k_{2D}^{1-|n_i|}}, \tag{8}$$

where

$$k_{2D} = \frac{2\pi f_{sc}}{V_{SW} \sin \Theta_{BR}} \tag{9}$$

is the 2D wavevector with projection at the spacecraft-frame frequency f_{sc},

$$k_{1D} = \frac{2\pi f_{sc}}{V_{SW} \cos \Theta_{BR}} \tag{10}$$

is the field-aligned wavevector with the same projection, and $r' = C_{2D}/C_{1D}$ is the ratio of energy associated with the 2D and 1D field-aligned components. From this, we quote $R_{1D} = C_{1D}/(C_{1D} + C_{2D}) = (1 + r')^{-1}$, which is the fraction of power in the 1D component. Note that in the examples show in Figure 1, $P_{YY} > P_{XX}$ consistently, and this remains a characteristic of the observations studied here. The variation of P_{YY}/P_{XX} with Θ_{BR} determines the ratio C_{1D}/C_{2D}, the ratio $P_{YY}/P_{XX} = 1$ at $\Theta_{BR} = 0°$, and the absolute value of the spectral index $|n|$ at 90°.

The assumption here is that the geometry of the turbulence in the plasma frame is invariant under rotation about the mean magnetic field direction. The ratio $P_{YY}/P_{XX} \neq 1$ is therefore a direct result of the measurement and is not representative of the underlying anisotropy of the magnetic fluctuation in the plasma frame, which is assumed to be one in the perpendicular plane (Bieber et al. 1996). It is also consistent with the Maltese Cross correlation function that is built from many samples of turbulence that span the range of mean field directions (Matthaeus et al. 1990; Dasso et al. 2005). The measured Θ_{BR} variation of Equation (8) can be fit to obtain the underlying statistical anisotropy of the energy as distributed to the parallel and perpendicular wavevectors using a single spacecraft. It has been used as a measurement of the relative amount of energy associated with the 1D (field-aligned) and 2D wavevectors, without regard for assuming specific wave dynamics (Bieber et al. 1996; Leamon et al. 1998a; Hamilton et al. 2008; MacBride et al. 2010). It can also be used to explain the result of Belcher & Davis (1971), where $P_{YY}/P_{XX} \simeq 1.25$, indicating an 80:20 distribution of energy associated with the 2D and 1D wavevectors.

Figure 11 shows our analysis of P_{YY}/P_{XX} for the data intervals that display a discernible spectral break marking the

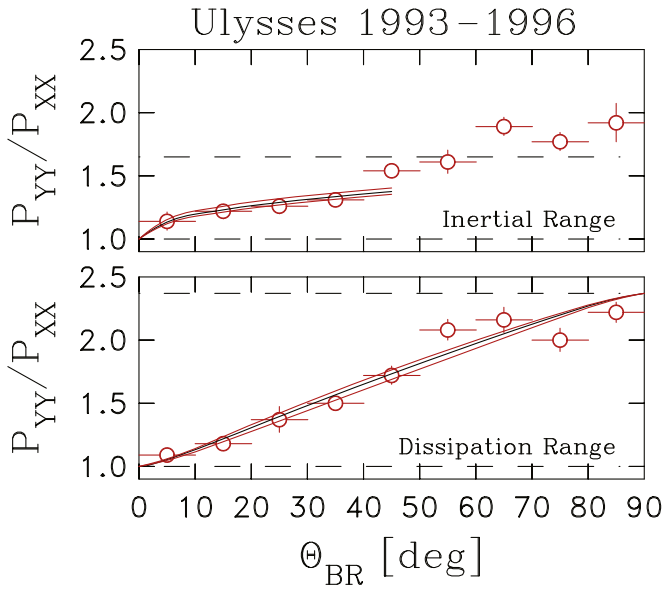

Figure 11. Mean value of P_{YY}/P_{XX} as computed within 10° bins for both inertial range frequencies (top) and dissipation-range frequencies (bottom). The best fit for the Bieber et al. (1996) analysis is shown by the black curves imposing $P_{YY}/P_{XX} = 1$ for $\Theta_{BR} = 0°$ and the average spectral index $|n|$ for $\Theta_{BR} = 90°$. The red lines represent the computed uncertainty in the best fit.

onset of dissipation. Figure 11 (top) shows our analysis of inertial range frequencies. The horizontal dashed lines are at 1 and 1.65, which represent the nominally expected values of P_{YY}/P_{XX} at $\Theta_{BR} = 0°$ and 90°, respectively. The symbols represent the unweighted mean value of P_{YY}/P_{XX} computed within 10° bins. The uncertainties in the measured averages are the error of the mean and are sometimes smaller than the circle symbols. The average ratio of P_{YY}/P_{XX} exceeds the theoretical limit for $\Theta_{BR} > 60°$ and this same behavior has been shown to be associated with compression in the Voyager data (Pine et al. 2020c). Therefore, we compute a best fit to the measurements for $\Theta_{BR} < 60°$ and get $R_{1D} = 0.35^{+0.04}_{-0.03}$ (=35%).

Figure 11 (bottom) shows our analysis of dissipation-range frequencies. The horizontal dashed lines are at 1 and 2.37, the latter being the mean of the absolute values of the dissipation-range indexes. Note that the average spectral index of the dissipation range rises (flattens) with increasing Θ_{BR} (see Figure 8). This is not taken into account in the fitting. The analysis is the same as above, except we use the full range of Θ_{BR}, because the large-angle values no longer exceed the limits of the theory. This is probably because the fluctuations in the dissipation scale are short-lived and less subject to compressive distortions. The best-fit value for the underlying anisotropy is $R_{1D} = 0.34^{+0.03}_{-0.02}$. The uncertainties in the two fits are sufficient to render them equivalent.

Table 1 summarizes past efforts to apply the single-spacecraft analysis of the underlying wavevector anisotropy as represented by Equation (8). (See also Table 1 in Oughton et al. 2015 for a similar summary.) Bieber et al. (1996) used this technique to study Helios observations from 0.3 to 1 au from 1 to 21 mHz and found that $R_{1D} = 0.26$. Interestingly, it is possible to apply the observation of energy-containing range fluctuations reported by Belcher & Davis (1971) and obtain $R_{1D} \simeq 0.20$, despite their interpretation that it demonstrates Alfvén waves with field-aligned wavevectors, because they use the same mean field coordinate system as Bieber et al. (1996). Leamon et al. (1998a) examined WIND observations and found that the inertial range had $R_{1D} = 11\%$ while the dissipation range had $R_{1D} = 0.46$. The suggested explanation for this was that there are a multitude of possible dissipation processes that can alter the underlying geometry in the dissipation range. A subsequent analysis found that the underlying geometry of the dissipation range within magnetic clouds had $R_{1D} \simeq 0.04$, suggesting that the dissipation of field-aligned wavevectors is much stronger in low-β_P conditions (Leamon et al. 1998b). Hamilton et al. (2008) divided fast- and slow-wind observations at 1 au in addition to magnetic clouds. They found that in fast-wind open-field observations, the inertial range had $R_{1D} = 0.45$, while the dissipation range had $R_{1D} = 0.82$. They also found that the slow-wind open-field observations had average inertial range values of $R_{1D} = 0.52$, while the dissipation range had $R_{1D} = 0.94$. Last, unlike Leamon et al. (1998b), they found that the inertial range in magnetic clouds had $R_{1D} = 0.57$, while the dissipation range had $R_{1D} = 1.00$. The Hamilton et al. (2008) results all have 1%–2% uncertainty owing to the size of the ensemble and standard deviations about 20% of the mean for dissipation-range values. MacBride et al. (2010) studied inertial range fluctuations observed by Helios 1 from 0.3 to 1 au and found results consistent with both Hamilton et al. (2008) and this paper. It is therefore notable that the change in the relative energy content of field-aligned wavevectors is small here when passing from the inertial to the dissipation range.

This analysis stands out, in that the computed geometry in the inertial and dissipation ranges is approximately equal. There are at least several reasons for the underlying wavevector geometry to differ between the two frequency ranges. The first possibility is undersampling, but data intervals with similar values of Θ_{BR} are not clustered in this analysis. The lack of clustering suggests statistical independence between individual samples. The nonlinear dynamics that support the energy-conserving inertial range tend to move energy into the 2D component, but large-scale dynamics such as shear and expansion may affect this transport. High-latitude solar minimum flow is noted for uniformity and has a lesser degree of transient behavior than low-latitude flow, so it is possible that this result is a better measure of turbulent dynamics, apart from the distortion effects of flow gradients. Dissipation dynamics favor either the 1D or 2D wavevectors, depending on the specific mechanism, so that the resulting dissipation-range geometry tends toward what wavevectors are least aggressively dissipated. We do not have a specific dissipation process identified in this analysis, so we can only note that whatever is happening in the dissipation range appears to apply to a broad range of wavevectors quasi-uniformly.

8. Discussion

The analysis presented here focuses almost exclusively on high-latitude magnetic field measurements recorded during solar minimum. Both the advantage and the challenge of that selection is that it is possible to construct an ensemble of measurements under nearly identical solar wind conditions. This means that some analyses benefit from a coalescence of statistical results, while other analyses lack the diversity needed to recognize trends and dependencies in the data. A good example of this is the ability to predict the onset of the dissipation spectrum and the inability to determine which physical parameter is responsible for that onset. At the same

Table 1
Single-spacecraft Geometry Analyses

References	Comment	R_{1D} Inertial Range	R_{1D} Dissipation Range
Belcher & Davis (1971)	Implied energy-range anisotropy	$\simeq 0.20$	⋯
Bieber et al. (1996)	Helios 1–21 mHz	0.26	⋯
Leamon et al. (1998a)	WIND spacecraft	$0.11^{+0.20}_{-0.11}$	$0.46^{+0.13}_{-0.11}$
Leamon et al. (1998b)	WIND magnetic clouds	$0.29^{+0.29}_{-0.29}$	$0.04^{+0.25}_{-0.04}$
Hamilton et al. (2008)	ACE all open fields	$0.53^{+0.01}_{-0.01}$	$0.83^{+0.01}_{-0.01}$
Hamilton et al. (2008)	ACE slow open fields	$0.52^{+0.01}_{-0.01}$	$0.94^{+0.01}_{-0.01}$
Hamilton et al. (2008)	ACE fast open fields	$0.45^{+0.02}_{-0.02}$	$0.82^{+0.01}_{-0.01}$
Hamilton et al. (2008)	ACE magnetic clouds	$0.57^{+0.01}_{-0.01}$	$1.00^{+0.01}_{-0.01}$
MacBride et al. (2010)	Helios 1 all winds	$0.27^{+0.12}_{-0.12}$	⋯
MacBride et al. (2010)	Helios 1 fast winds	$0.33^{+0.21}_{-0.17}$	⋯
MacBride et al. (2010)	Helios 1 slow winds	$0.16^{+0.20}_{-0.15}$	⋯
This paper	Ulysses fast open fields	$0.35^{+0.04}_{-0.03}$	$0.34^{+0.03}_{-0.02}$

time, the ensemble does not represent the same measurement repeated many times. The ability to observe the dependence of the dissipation-range spectral index upon the strength of the turbulence demonstrates this fact.

Some results show a trend toward agreement with earlier 1 au near-ecliptic observations without providing sufficient resolution of that trend. The dependence of the variance anisotropy on β_P is one such example where the measurements fail to provide sufficient variability to say conclusively whether there is agreement.

Hamilton et al. (2008) offered an interpretation of the larger fraction of slab energy in the dissipation range for low latitudes. First, they noted that the 2D portion is much larger in the inertial range than in the slab portion. Second, based on MHD and kinetic simulations and analyses, turbulent energy cascades are preferentially in the direction perpendicular to the mean magnetic field. So this larger 2D energy is expected to continue into the dissipation range as 2D wavevector fluctuations. To find the slab dominating the 2D fluctuations in the dissipation range implies that the 2D energy from the inertial range is dissipated greatly in a small neighborhood of frequencies around the spectral break. Slab fluctuations dissipate far less over the same range of frequency and so dominate the dissipation range.

At high latitudes during solar minimum, our results indicate that the slab fraction does not differ much between the inertial and dissipation ranges. Following Hamilton et al. (2008), this suggests that the damping of the 2D and slab fluctuations occurs in the same range of frequencies and by approximately similar amounts.

Why these differences are found between low-latitude and high-latitude fluctuations is not presently known. Two possible explanations can be given. First, plasma β is smaller on average at low latitudes than at high latitudes. Compressions associated with fluctuations have been theorized to alter interplanetary fluctuation polarization and spectral magnetic helicity (Markovskii & Vasquez 2016; Markovskii et al. 2016). The helicity, in particular, is a function of plasma β. Compressions might also influence anisotropy, especially in so far as it presents additional dissipation mechanisms. Second, the relative magnetic field amplitude of fluctuations is typically smaller for low latitudes than for high latitudes. Particle-in-cell simulations of turbulence find that electron heating is more effective for small relative amplitude, whereas at large amplitude ion heating dominates (Wu et al. 2013; Roy et al. 2022; Yang et al. 2023). Therefore, the dissipation mechanism could vary with relative amplitude and become associated with differing anisotropy.

9. Summary

We have examined the properties of the dissipation range in the magnetic power spectra as seen by Ulysses at high latitudes during solar minimum over the years 1993–1996. Although we began with 284 data intervals that were carefully chosen to be outside the influence of transients, we focus on the magnetic power spectra of 119 data intervals that show clear evidence of a spectral break in association with the onset of dissipation. As has been seen in other spacecraft observations, the onset of dissipation scales with both the proton cyclotron and inertial scales. Solar wind plasma parameters are too closely correlated to distinguish between the two scales.

As the magnetic power level increases, the dissipation range steepens. The magnetic power is one of several contributions to the rate of energy transport through the inertial range ϵ, and the correlation between the energy transport rate and the spectral slope of the dissipation range continues here (Smith et al. 2006a).

An unexpected result is the observation that the variance anisotropy in the dissipation and inertial ranges are nearly identical. There is a slight dependence for the dissipation-range result on the energy transport rate and possibly other parameters, but it is slight enough that the general equality between the anisotropy of the two ranges holds.

We do find the familiar result where the fraction of magnetic energy associated with field-aligned wavevectors increases within the dissipation range relative to inertial range scales (Hamilton et al. 2008), but the increase is marginal. The 1D component of the inertial range wavevector anisotropy is less than, but comparable to, what we find for the ACE observations at 1 au, but the relative energy content associated with field-aligned wavevectors in the dissipation range is lower here than in the ACE data. This means that the dissipation-range energy lies within the 2D plane to a greater degree in the Ulysses data than in the ecliptic at 1 au. Especially when comparing fast-wind observations, this means that both the inertial and dissipation ranges are more nearly 2D in the high-latitude solar minimum Ulysses data than in the ACE data.

Acknowledgments

C.W.S. and P.A.I. were supported by NASA grant NNX17AB86G. C.W.S., B.J.V., P.A.I., A.S.W., and A.V.M. were supported by NASA HSR grant 80NSSC18K1215. C.W.S., B.J.V., P.A.I., and N.A.S. were partially supported by NASA grant 80NSSC17K0009. P.A.I. and B.J.V. are supported by NSF grant AGS2005982. B.J.V. is supported by NASA grants 80NSSC19K0832 and 80NSSC21K1674. C.J.J. and N.A.S. are supported by the Interstellar Boundary Explorer mission as a part of NASA's Explorer Program, partially by NASA SR&T Grant NNG06GD55G, and the Sun-2-Ice (NSF grant No. AGS1135432) project. The data used in this analysis are available from the National Space Science Data Center.

Appendix
Time Interval Listings

The data intervals used here were originally selected to provide control intervals for a study of wave excitation by newborn interstellar He^+ from 1990 to 2009 (Marchuk et al. 2021). To serve as control intervals, they are required to not display evidence of wave excitation at frequencies near the He^+ cyclotron frequency. To serve as examples of turbulence without complication by waves excited by suprathermal ions, we also require that there be no evidence of wave excitation at the frequencies near the H^+ cyclotron frequency. Most of these intervals were also used in an earlier study of inertial range spectra during these same years 1993–1996 (Watson et al. 2022).

Table 2 lists the 119 time intervals used in this study that display a clear spectral break in association with the onset of dissipation. Table 3 lists the 165 intervals that do not display a clear spectral break. There are instances where two overlapping time intervals are selected for the same day. We find that these overlapping intervals can display significant differences in the spectra and have chosen to include them separately in this study.

Table 2
Ulysses Observations with Spectral Breaks

Year	Time (DOY::Hour:Min)	Time (DOY::Hour:Min)	Time (DOY::Hour:Min)	Time (DOY::Hour:Min)
1993	003/02:00–14:01	024/00:00–12:00	028/16:01–21:01	107/00:00–12:00
	147/00:00–11:01	147/00:00–12:00	180/00:00–12:00	180/02:00–12:00
	241/07:00–14:01	245/07:00–19:00	268/00:00–12:00	341/00:00–12:00
	350/00:00–12:00	353/01:00–08:00	360/02:00–16:01	…
1994	007/12:01–07:20	008/12:01–20:01	009/12:00–20:01	010/12:00–19:00
	027/11:00–19:00	051/03:00–07:01	067/08:00–17:00	071/09:01–16:01
	073/00:00–12:00	074/15:01–23:02	164/01:00–09:01	185/09:01–19:00
	193/00:00–07:00	207/09:01–19:00	232/00:00–07:00	235/00:00–07:00
	274/00:00–21:01	277/00:00–19:00	280/00:00–16:01	285/00:00–14:01
	290/00:00–12:00	293/03:01–13:00	296/00:00–14:01	301/13:00–19:00
	303/00:00–13:00	325/10:02–19:00	329/12:00–21:01	341/00:00–12:00
	344/00:00–15:01	353/12:00–21:01	355/04:01–12:00	357/01:00–12:00
	361/06:01–10:01	…	…	…
1995	019/02:01–07:02	046/07:00–19:00	059/18:00–23:02	060/09:01–19:00
	072/12:00–21:01	092/18:00–23:02	112/09:01–23:02	135/07:00–21:01
	138/02:00–16:01	147/07:00–21:01	158/09:01–19:00	163/19:01–22:01
	167/10:02–22:01	168/09:01–21:01	169/19:01–23:02	175/17:01–23:02
	177/09:01–21:01	181/16:00–23:02	182/04:01–19:00	183/13:00–23:02
	187/12:00–23:02	189/14:01–23:02	190/07:02–23:02	196/15:00–23:02
	198/02:00–14:01	203/19:00–23:00	203/12:00–23:02	207/14:01–23:02
	210/17:01–23:02	217/16:01–23:02	218/14:01–23:02	220/18:00–23:02
	222/02:00–14:01	235/17:00–23:02	236/18:01–23:02	239/04:01–19:00
	242/17:01–23:02	243/00:00–12:00	243/04:01–10:02	244/00:00–04:01
	246/15:01–22:01	255/00:00–04:01	256/16:01–23:02	257/00:00–04:01
	260/16:01–23:02	274/02:00–07:00	303/09:01–12:01	339/00:00–16:01
	347/00:00–16:01	…	…	…
1996	013/03:01–09:01	014/12:01–23:01	015/02:00–08:00	020/21:01–23:02
	024/01:01–09:01	029/09:01–16:01	030/00:00–23:02	031/02:02–11:00
	032/09:01–23:02	050/07:02–13:02	081/09:01–23:02	084/04:01–14:01
	085/19:00–23:02	100/19:00–23:02	105/15:01–23:02	121/13:02–22:01
	152/15:01–22:00	158/04:01–10:01	158/02:00–12:00	182/00:00–12:00
	198/09:01–18:01	…	…	…

Note. This table contains entries from Table 1 of Watson et al. (2022).

Table 3
Ulysses Observations without Spectral Breaks

Year	Time (DOY::Hour:Min)	Time (DOY::Hour:Min)	Time (DOY::Hour:Min)	Time (DOY::Hour:Min)
1993	010/00:00–07:00	028/00:01–09:01	034/00:00–12:00	034/00:00–14:01
	043/04:01–12:00	044/03:01–11:01	057/00:00–02:00	058/11:01–14:01
	060/16:01–23:02	068/09:01–16:01	068/04:01–16:01	084/02:00–07:01
	097/04:01–16:01	117/12:00–21:01	126/00:00–06:01	140/04:01–19:00
	141/02:00–12:00	150/12:00–23:02	151/02:00–12:00	157/12:00–18:01
	172/00:00–12:00	192/02:00–16:01	192/04:01–16:01	229/07:00–18:01
	229/02:00–16:01	239/04:01–18:02	251/04:01–16:01	269/07:00–10:00
	277/02:00–11:00	277/00:00–12:00	280/00:00–09:00	289/00:00–12:00
	294/07:00–16:01	296/02:00–15:01	312/02:00–19:00	324/04:01–14:01
	326/03:00–06:00	330/00:00–12:00	334/00:00–13:01	361/00:02–10:00
	361/02:00–12:00	…	…	…
1994	003/00:01–06:01	013/00:00–12:00	027/00:00–09:01	041/10:02–19:01
	047/07:00–09:01	062/12:00–21:01	074/00:00–07:00	078/00:00–12:00
	085/12:00–23:02	093/00:00–12:00	110/10:02–16:01	110/12:00–21:01
	112/10:02–23:01	128/09:01–23:02	134/13:00–23:01	136/17:01–22:01
	139/12:00–23:02	151/12:01–18:00	154/12:00–23:02	157/11:00–15:02
	163/12:00–19:00	163/12:00–23:01	173/16:01–23:02	183/09:01–19:01
	197/09:01–19:01	206/12:00–19:00	209/09:01–13:01	209/07:00–14:01
	219/07:00–19:00	224/12:00–18:00	241/07:00–19:00	256/09:01–14:02
	313/00:00–12:00	364/12:01–17:00	364/12:00–21:01	…
1995	004/09:01–19:00	007/13:02–16:01	011/12:01–17:01	011/12:00–23:02
	015/12:00–20:01	016/12:00–19:00	017/00:00–04:01	018/12:00–19:00
	023/13:00–19:01	024/09:01–21:01	027/12:00–19:00	028/09:01–19:00
	034/12:00–20:01	035/00:00–06:00	046/16:01–18:01	046/07:00–19:00
	074/15:01–22:01	075/09:01–19:00	076/09:01–19:00	077/00:01–03:02
	081/18:00–23:02	081/09:01–23:02	089/15:01–22:00	094/19:00–23:02
	101/02:00–19:00	127/04:01–19:00	222/19:00–23:02	231/14:01–23:02
	234/13:01–23:02	238/16:01–23:02	243/13:00–20:01	249/02:00–15:01
	254/15:00–23:02	259/04:01–14:01	266/00:00–09:00	267/08:00–13:00
	267/09:01–21:01	272/01:00–10:00	273/01:00–12:00	278/04:01–14:01
	280/03:00–06:00	280/01:00–15:01	297/00:00–16:01	302/00:00–16:01
	321/09:01–21:01	336/00:02–03:01	340/00:00–02:01	356/00:00–12:00
1996	005/09:01–23:02	011/14:01–21:01	018/18:01–20:01	018/14:01–23:02
	023/09:01–23:02	030/02:00–06:00	043/09:01–23:02	058/09:01–23:02
	061/07:00–19:00	073/00:00–04:00	085/03:01–09:01	091/05:00–13:01
	094/13:01–17:01	094/07:00–19:00	098/09:02–11:01	098/04:01–14:01
	100/05:01–09:01	115/09:01–12:00	116/00:00–16:01	118/02:00–15:01
	131/03:01–12:00	136/05:00–07:00	141/00:01–03:00	150/07:00–13:02
	185/00:00–12:00	201/03:02–07:02	201/00:00–09:01	213/03:00–05:00
	217/00:01–03:00	231/09:01–23:02	239/00:00–02:00	276/16:01–18:02
	300/00:00–16:01	306/04:01–07:00	308/04:01–07:00	317/12:00–23:02
	347/07:00–19:00	353/14:01–23:02	…	…

Note. This table contains entries from Table 1 of Watson et al. (2022).

ORCID iDs

Charles W. Smith https://orcid.org/0000-0002-5379-1542
Matthew R. Argall https://orcid.org/0000-0001-6315-1613
Colin J. Joyce https://orcid.org/0000-0002-3841-5020
Philip A. Isenberg https://orcid.org/0000-0003-0505-8546
Bernard J. Vasquez https://orcid.org/0000-0001-8593-7289
Nathan A. Schwadron https://orcid.org/0000-0002-3737-9283

References

Aggarwal, P., Taylor, D. K., Smith, C. W., et al. 2016, ApJ, 822, 94
Argall, M. R., Fisher, M. F., Joyce, C. J., et al. 2015, GeoRL, 42, 9617
Argall, M. R., Hollick, S. J., Pine, Z. B., et al. 2017, ApJ, 849, 61
Argall, M. R., Hollick, S. J., Pine, Z. B., et al. 2018, ApJ, 854, 77
Bale, S. D., Kellogg, P. J., Mozer, F. S., Horbury, T. S., & Reme, H. 2005, PhRvL, 94, 215002
Batchelor, G. K. 1953, The Theory of Homogeneous Turbulence (Cambridge: Cambridge Univ. Press)
Belcher, J. W., & Davis, L., Jr. 1971, JGR, 76, 3534
Beresnyak, A. 2011, PhRvL, 106, 075001
Bieber, J. W., Wanner, W., & Matthaeus, W. H. 1996, JGR, 101, 2511
Blackman, R. B., & Tukey, J. W. 1958, The Measurement of Power Spectra (New York: Dover),
Boldyrev, S. 2006, PhRvL, 96, 115002
Boldyrev, S., Mason, J., & Cattaneo, F. 2009, ApJL, 699, L39
Bruno, R., & Trenchi, L. 2014, ApJL, 787, L24
Bruno, R., Trenchi, L., & Telloni, D. 2014, ApJL, 793, L15
Cannon, B. E., Smith, C. W., Isenberg, P. A., et al. 2013, in AIP Conf. Proc. 1539, Solar Wind 13 (Melville, NY: AIP), 334
Cannon, B. E., Smith, C. W., Isenberg, P. A., et al. 2014a, ApJ, 784, 150
Cannon, B. E., Smith, C. W., Isenberg, P. A., et al. 2014b, ApJ, 787, 133
Cannon, B. E., Smith, C. W., Isenberg, P. A., et al. 2017, ApJ, 840, 13

Chen, C. H. K., Horbury, T. S., Schekochihin, A. A., et al. 2010a, PhRvL, 104, 255002
Chen, C. H. K., Leung, L., Boldyrev, S., Maruca, B. A., & Bale, S. D. 2014, GeoRL, 41, 8081
Chen, C. H. K., Wicks, R. T., Horbury, T. S., & Schekochihin, A. A. 2010b, ApJL, 711, L79
Chen, J. 1989, PhD thesis, Univ. of Del., Newark
Cho, J., & Vishniac, E. T. 2000, ApJ, 539, 273
Dasso, S., Milano, L. J., Matthaeus, W. H., & Smith, C. W. 2005, ApJL, 635, L181
Ercoline, L. A., Smith, C. W., Argall, M. R., et al. 2023, ApJ, 945, 168
Fisher, M. K., Argall, M. R., Joyce, C. J., et al. 2016, ApJ, 830, 47
Forman, M., Wicks, R. T., & Horbury, T. S. 2011, ApJ, 733, 76
Fowler, R. A., Kotick, B. J., & Elliott, R. D. 1967, JGR, 72, 2871
Goldreich, P., & Sridhar, S. 1995, ApJ, 438, 763
Goldstein, M. L., Roberts, D. A., & Matthaeus, W. H. 1995, ARA&A, 33, 283
Hamilton, K., Smith, C. W., Vasquez, B. J., & Leamon, R. J. 2008, JGRA, 113, A01106
He, J., Marsch, E., Tu, C., Yao, S., & Tian, H. 2011, ApJ, 731, 85
Hollick, S. J., Smith, C. W., Pine, Z. B., et al. 2018a, ApJ, 863, 75
Hollick, S. J., Smith, C. W., Pine, Z. B., et al. 2018b, ApJ, 863, 76
Hollick, S. J., Smith, C. W., Pine, Z. B., et al. 2018c, ApJS, 237, 34
Horbury, T. S., Forman, M., & Oughton, S. 2008, PhRvL, 101, 175005
Howes, G. G., Dorland, W., Cowley, S. C., et al. 2008, PhRvL, 100, 065004
Howes, G. G., & Quataert, E. 2010, ApJL, 709, L49
Hughes, R. S., Gary, S. P., Wang, J., & Parahar, T. N. 2017, ApJL, 847, L14
Iroshnikov, P. S. 1964, SvA, 7, 566
Isenberg, P. A., & Vasquez, B. J. 2019, ApJ, 63, 887
Joyce, C. J., Smith, C. W., Isenberg, P. A., Murphy, N., & Schwadron, N. A. 2010, ApJ, 724, 1256
Kolmogorov, A. N. 1941, Dokl. Akad. Nauk SSSR, 30, 301, (Reprinted in Proc. R. Soc. London A, 434, 9-13, 1991)
Kraichnan, R. H. 1965, PhFl, 8, 1385
Leamon, R. J., Smith, C. W., Ness, N. F., Matthaeus, W. H., & Wong, H. K. 1998a, JGR, 103, 4775
Leamon, R. J., Smith, C. W., Ness, N. F., & Wong, H. K. 1999, JGR, 104, 344
Leamon, R. J., Smith, C. W., & Ness, N. F. 1998b, GeoRL, 25, 2505
MacBride, B. T., Smith, C. W., & Vasquez, B. J. 2010, JGR, 115, A07105
Marchuk, A. V., Smith, C. W., Watson, A. S., et al. 2021, ApJ, 923, 185
Markovskii, S. A., & Vasquez, B. J. 2011, ApJ, 739, 22
Markovskii, S. A., & Vasquez, B. J. 2016, ApJ, 820, 15
Markovskii, S. A., Vasquez, B. J., & Smith, C. W. 2008, ApJ, 675, 1576
Markovskii, S. A., Vasquez, B. J., & Smith, C. W. 2015, ApJ, 806, 78
Markovskii, S. A., Vasquez, B. J., & Smith, C. W. 2016, ApJ, 833, 212
Matthaeus, W. H., Ghosh, S., Oughton, S., & Roberts, D. A. 1996a, JGR, 101, 7619
Matthaeus, W. H., & Goldstein, M. L. 1982a, JGR, 87, 6011
Matthaeus, W. H., & Goldstein, M. L. 1982b, JGR, 87, 10347
Matthaeus, W. H., Goldstein, M. L., & Roberts, D. A. 1990, JGR, 95, 20673
Matthaeus, W. H., Goldstein, M. L., & Smith, C. W. 1982, PhRvL, 48, 1256
Matthaeus, W. H., Oughton, S., Ghosh, S., & Hossain, M. 1998, PhRvL, 81, 2056
Matthaeus, W. H., Parashar, T. N., Wan, M., & Wu, P. 2016, ApJL, 827, L7
Matthaeus, W. H., & Zhou, Y. 1989, PhFlB, 1, 1929
Means, J. D. 1972, JGR, 77, 5551
Mish, W. H., Wenger, R. M., Behannon, K. W., & Byrnes, J. B. 1982, Interactive Digital Signal Processor, NASA Technical Memorandum 83997, Goddard Space Flight Center, Greenbelt, MD
Müller, W.-C., & Grappin, R. 2005, PhRvL, 95, 114502
Oughton, S., Matthaeus, W. H., Wan, M., & Osman, K. T. 2015, RSPTA, 373, 20140152
Oughton, S., Priest, E. R., & Matthaeus, W. H. 1994, JFM, 280, 95
Parashar, T. N., Shay, M. A., Cassak, P. A., & Matthaeus, W. H. 2009, PhPl, 16, 032310
Parker, E. N. 1963, Interplanetary Dynamical Processes (New York: Wiley-Interscience)
Pine, Z. B., Smith, C. W., Hollick, S. J., et al. 2020a, ApJ, 900, 91
Pine, Z. B., Smith, C. W., Hollick, S. J., et al. 2020b, ApJ, 900, 92
Pine, Z. B., Smith, C. W., Hollick, S. J., et al. 2020c, ApJ, 900, 93
Pine, Z. B., Smith, C. W., Hollick, S. J., et al. 2020d, ApJ, 900, 94
Pine, Z. B., Smith, C. W., Hollick, S. J., et al. 2020e, ApJS, 250, 14
Roy, S., Bandyopadhyay, R., Yang, Y., et al. 2022, ApJ, 941, 137
Šafránková, J., Němeček, Z., Přech, L., & Zastenker, G. N. 2013, PhRvL, 110, 025004
Sahraoui, F., Goldstein, M. L., Belmont, G., Canu, P., & Rezeau, L. 2010, PhRvL, 105, 131101
Sahraoui, F., Goldstein, M. L., Robert, P., & Khotyaintsev, Y. 2009, PhRvL, 102, 231102
Servidio, S., Osman, K. T., Valentini, F., et al. 2014, ApJL, 781, L27
Servidio, S., Valentini, F., Califano, F., & Veltri, P. 2012, PhRvL, 108, 045001
Servidio, S., Valentini, F., Perrone, D., et al. 2015, JPlPh, 81, 325810107
Shebalin, J. V., Matthaeus, W. H., & Montgomery, D. 1983, JPlPh, 29, 525
Smith, C. W., Aggarwal, P., Argall, M. R., et al. 2017, JPhCS, 900, 012018
Smith, C. W., Hamilton, K., Vasquez, B. J., & Leamon, R. J. 2006a, ApJL, 645, L85
Smith, C. W., Isenberg, P. A., Matthaeus, W. H., & Richardson, J. D. 2006b, ApJ, 638, 508
Smith, C. W., Vasquez, B. J., & Hamilton, K. 2006c, JGRA, 111, A09111
Stawarz, J. E., Smith, C. W., Vasquez, B. J., Forman, M. A., & MacBride, B. T. 2009, ApJ, 697, 1119
Taylor, G. I. 1935, RSPSA, 151, 421
TenBarge, J. M., Howes, G. G., & Dorland, W. 2013, ApJ, 744, 139
Valentini, F., Perrone, D., Stabile, S., et al. 2016, NJPh, 18, 125001
Vasquez, B. J., & Markovskii, S. A. 2012, ApJ, 747, 19
Vasquez, B. J., Smith, C. W., Hamilton, K., MacBride, B. T., & Leamon, R. J. 2007, JGRA, 112, A07101
Watson, A. S., Smith, C. W., Marchuk, A. V., et al. 2022, ApJ, 927, 43
Woodham, L. D., Wicks, R. T., Verscharen, D., & Owen, C. J. 2018, ApJ, 856, 49
Woodham, L. D., Wicks, R. T., Verscharen, D., TenBarge, J. M., & Howes, G. G. 2021, ApJ, 912, 101
Wu, P., Wan, S. M., Matthaeus, W. H., Shay, M. A., & Swisdak, M. 2013, PhRvL, 111, 121105
Yang, Y., Pecora, F., Matthaeus, W. H., et al. 2023, ApJ, 944, 148